

JGR Solid Earth

RESEARCH ARTICLE

10.1029/2020JB021037

Key Points:

- A magnetic record of the Eocene section near Tibet reveals a one and a half million yearlong aridity
- The aridity interval 45.5–44 Ma coincides with aridity maximum in inner Asia
- The middle Eocene aridity coincides with cooling registered in oceanic records

Correspondence to:

V. A. Kravchinsky,
vadim@ualberta.ca

Citation:

Zhang, R., Kravchinsky, V. A., Qin, J., Goguitchaichvili, A., & Li, J. (2021). One and a half million yearlong aridity during the middle Eocene in north-west China linked to a global cooling episode. *Journal of Geophysical Research: Solid Earth*, 126, e2020JB021037. <https://doi.org/10.1029/2020JB021037>

Received 21 SEP 2020

Accepted 29 JAN 2021

One and a Half Million Yearlong Aridity During the Middle Eocene in North-West China Linked to a Global Cooling Episode

Rui Zhang^{1,2,3,4} , Vadim A. Kravchinsky^{1,2} , Jie Qin^{1,2}, Avto Goguitchaichvili⁵, and Jianxing Li⁶

¹Department of Geology, Institute of Cenozoic Geology and Environment, State Key Laboratory of Continental Dynamics, Northwest University, Xi'an, China, ²Department of Physics, Geophysics, University of Alberta, Edmonton Alberta, Canada, ³State Key laboratory of Loess and Quaternary Geology, Institute of Earth Environment, Chinese Academy of Sciences, Xi'an, China, ⁴CAS Center for Excellence in Quaternary Science and Global, Chinese Academy of Sciences, Xi'an, China, ⁵Servicio Arqueomagnético Nacional, Instituto de Geofísica, Universidad Nacional Autónoma de México, Campus Morelia, Morelia, Mexico, ⁶Chengdu Center of Geological Survey, China Geological Survey, Chengdu, China

Abstract The Eocene record of substantial aridification near Tibet was reported to mimic the global climate cooling trend, overwriting the previously proposed dominant role of the Tibetan Plateau uplift in the aridification (Li et al., 2018, <https://doi.org/10.1038/s41467-018-05415-x>). Here we present new paleoclimate data from the red clay sequence deposited between 40 and 50 Ma in Altun Shan at the northeastern edge of the Tibetan Plateau. After building an age model using a compilation of magnetostratigraphy and cyclostratigraphy, we demonstrate that our record of magnetic susceptibility in the Altun Shan red clay exhibits variations linked to eccentricity cycles. Our age model allows us to estimate the age of eight short geomagnetic events, cryochrons, in Altun Shan. Further we show that the aridification interval in Altun Shan coincides with (i) a cooling event recorded in the global oxygen isotope record, (ii) a sea surface temperature record on the east Tasmanian plateau, and (iii) an aridity record in the surrounding sedimentary basins of Central Asia. The middle Eocene aridity and cooling reached its maximum 45.5–44 Ma.

Plain Language Summary Two notable Eocene climate warming events are extensively discussed in the literature—the middle Eocene climatic optimum and the early Eocene climatic optimum. Here, we report our accurately dated climate proxy record of magnetic parameters from the Altun Shan red clay section at the northeastern part of the Tibetan Plateau that reveals an aridity interval 45.5–44 Ma. The Altun Shan magnetic susceptibility record, an indicator of aridity vs. moisture intensification intervals, exhibits variations linked to eccentricity cycles. The one and a half million yearlong aridity event in Altun Shan coincides with the aridity in middle Asia and the cooling event that could be observed in the global oxygen isotope compilation and the first appearance of ice-rafted debris from Greenland and Pan-Arctic sources, indicating global distribution of aridity and cooling 45.5–44 Ma.

1. Introduction

The determination of driving mechanisms of global climate variations requires detailed sedimentary records that are rare for the Eocene in continental Eurasia. Li et al. (2018) described a unique continuous Eocene eolian section in Altun Shan situated in the eastern Xorkol basin in the northeastern Tibetan Plateau (91°31'45"E, 38°54'42"N) (Figure 1). The paleoclimatic proxy record of mass-specific frequency-dependent magnetic susceptibility (χ_{fd}) in the Altun Shan red clay sediment strongly resembles the global cooling trend registered in the oceanic oxygen isotope $\delta^{18}\text{O}$ reference record (Zachos et al., 2008); therefore, Li et al. (2018) concluded that Altun Shan enhanced aridification was a response to global climatic forcing rather than to the uplift of the Tibetan Plateau. The visual resemblance of the χ_{fd} and $\delta^{18}\text{O}$ curves motivated us to independently test the hypothesis that global cooling played a dominant role in Asian inland aridification by demonstrating the ability of the Eocene red clay sequence to record climate fluctuations paced by astronomical periodicities. Here we report new magnetic susceptibility (MS) measurements and additional paleomagnetic directions of samples from the Altun Shan section described in Li et al. (2018). MS is among

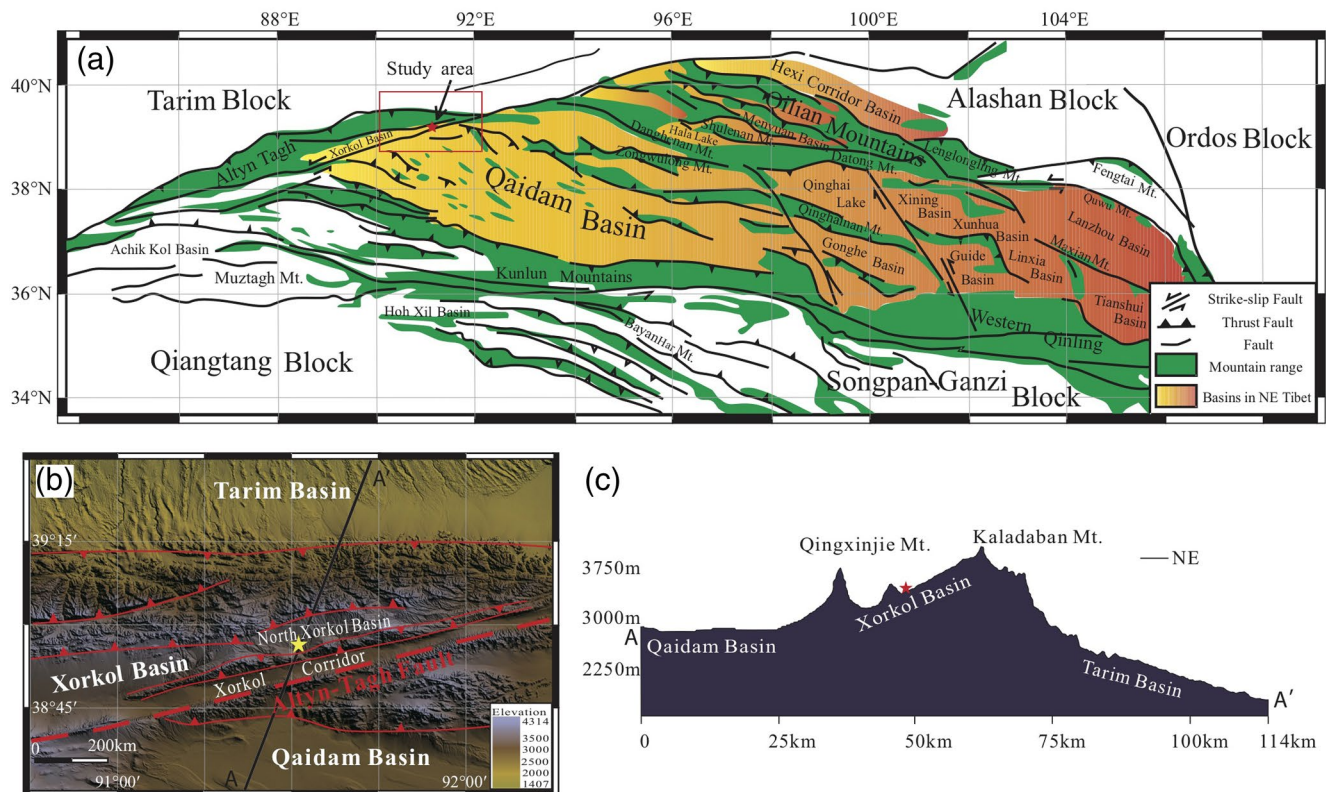


Figure 1. (a) Location of the Xorkol Basin and its relationship to the tectonic units and major faults in the study area (The Geological Survey Team, 1981). (b) Topographic map with major faults in the study location. A star indicates the red clay section reported in this manuscript. (c) Topographic profile A-A' across the studied location and the adjacent area in (b). A star indicates the sampling location.

the most effective climate proxy parameters in loess and red clay deposits in China because an increase in MS values corresponds to an increase in moisture and paleosol development (An et al., 2001), although Zhao et al. (2020) suggested that relatively strong pedogenesis and chemical weathering in the Late Oligocene to Early Miocene red clay deposits was influenced by higher temperature conditions rather than higher precipitation. It was demonstrated that magnetic grain-size distributions in paleosol sequences in Chinese loess and in red clay deposits are similar, indicating that MS can be used to indicate the intensity of the east Asian summer monsoon in red clay sequences (Nie et al., 2007, 2013; Zhao et al., 2016) and the aridity in the zone of influence by assessing the midlatitude westerly moisture variations (Li et al., 2018).

MS is sensitive to the concentration of ferrimagnetic minerals in the sediment, and is enhanced in red clay paleosols under warm and humid conditions due to the formation of fine-grained magnetite and maghemite (Zhao et al., 2016). MS is reported to increase with higher degree of pedogenesis in Chinese red clay deposits (Nie et al., 2007; Zhao et al., 2016). Li et al. (2018) demonstrated that magnetic properties of the red clay in the studied section are similar to those of Quaternary loess-paleosol sequences and other red clay sequences. Ultrafine ferrimagnetic grains produced during pedogenesis are responsible for an increase in magnetic susceptibility, therefore the MS enhancement mechanism in red clay sections in China is similar to that of the overlying loess-paleosol. The rock-magnetic data in Li et al. (2018, Supplementary Note 5) showed that the magnetic mineral assemblage for the studied section is fairly uniform and additionally to the fine-grained magnetite/maghemite contains coarse-grained magnetite and hematite. The amount of fine-grained magnetite/maghemite particles increases toward the lower portion of the section, which is older than ~47 Ma. Hematite becomes more noticeable in the upper part of the section.

It was shown that the MS signal could be an effective paleoclimate proxy in Chinese red clay deposits where Milankovitch climate cycles were reported using MS data (Anwar et al., 2015; Evans et al., 1991; Nie et al., 2008, 2011, 2018; Sun et al., 2006, 2010; Vandenberghe et al., 2004; Zhang et al., 2018). Therefore,

the MS signal creates a good basis to construct an astronomically tuned age model. The cyclostratigraphic approach we used in our study allows us to confirm which magnetostratigraphic age model from three different models suggested by Li et al. (2018) was the more suitable model. Additionally, the accurate age model allows assessing the age of the short geomagnetic polarity events, possible cryptochrons, in the Altun Shan study section.

Li et al. (2018) introduced three alternative magnetostratigraphy based age models for the Altun Shan section, considering some short polarity intervals as possible excursions. In the first age model, the authors (Li et al., 2018) selected an age model with smoother sedimentation rates that estimated the time span of the section to be between ~40 and 51 Ma. This age model produced a better match between the reported χ_{fd} curve and the oceanic $\delta^{18}O$ record (Zachos et al., 2008). The second age model (40–54 Ma) in Li et al. (2018) produced larger sedimentation rate variations but still matched well with the oceanic reference record (Zachos et al., 2008) and the age of mammalian fossils (Wang, 2017). The third age model (35–39 Ma) in Li et al. (2018) was based on a visual matching of the paleomagnetic polarity pattern with the geomagnetic polarity time scale (GPTS) (Gradstein et al., 2012), but the paleomagnetic polarity pattern was inconsistent with the age of mammalian fossils (Wang, 2017). The choice of age model is critical because it is the basis of the conclusion regarding the beginning of aridification in Asia.

Li et al. (2018) showed the multimillion-year climatic trend recorded in the frequency-dependent magnetic susceptibility that correlated with the global cooling. Frequency-dependent magnetic susceptibility (χ_{fd}) is a measure of ferrimagnetic nanoparticles with grain sizes from the superparamagnetic (SP) to stable single domain (SD) size range. It is well established for Chinese loess and red clay sections that χ_{fd} is enhanced in paleosols due to the formation of SP and SD magnetic particles in a warm and humid environment (Li et al., 2018). In our study we aimed to obtain finer variations in the MS time series to reconstruct more complex climate behavior in the Altun Shan red clay sequence and to assess an interval of global aridity and cooling in the middle Eocene.

2. Geological Setting

The studied Eocene eolian sequence, the Xishuigou Formation, is located in the eastern part of the Cenozoic Xorkol basin, which is delimited by high-angle reverse faults on both sides, deformed into an asymmetric syncline with a shallower northern limb and a deeper southern limb, and is overlain uncomfortably by Miocene sediments of the Caihonggou Formation (Li et al., 2014). *Yuomys altunesis* fossils of the middle-late Eocene age were contained in fine-grained sandstones and siltstones in the sections and described in Wang (2017) and Li et al. (2018). With a thickness of ~96 m, the sampling interval of the Xishuigou Formation was around 20 cm in ~40 eolian red clay layers interbedded with carbonate nodules. Ninety two percent of the red clay section that was studied was comprised of fine-grained eolian particles with grain size < 100 μm . Quartz grains of the original shape are well preserved in the sampled grains, indicating that they were transported by wind from the source (Li et al., 2018).

The red clay section contains typical eolian pseudobedding that consists of alternating red clay and calcareous nodule strata formed from leaching of the clay above (Figure 2). Layer-cutting, spindle-like calcareous nodules in numerous strata define pseudobedding; such feature is a characteristic of eolian, not aquatic, sediments.

3. Methods

3.1. Magnetic Susceptibility Measurements

The mass-specific low-field magnetic susceptibility ($10^{-8} \text{ m}^3/\text{kg}$) of each red clay section sample was measured using a KappaBridge KLY-4S magnetic susceptibility meter (Agico Ltd., Brno) with an automated sample handling system (428 samples).

3.2. Paleomagnetic Measurements

Paleomagnetic specimens were measured with a 2-G Enterprises cryogenic magnetometer 755-1.65 in the paleomagnetic laboratory of the North-west University in Xi'an, China. Demagnetizations were performed

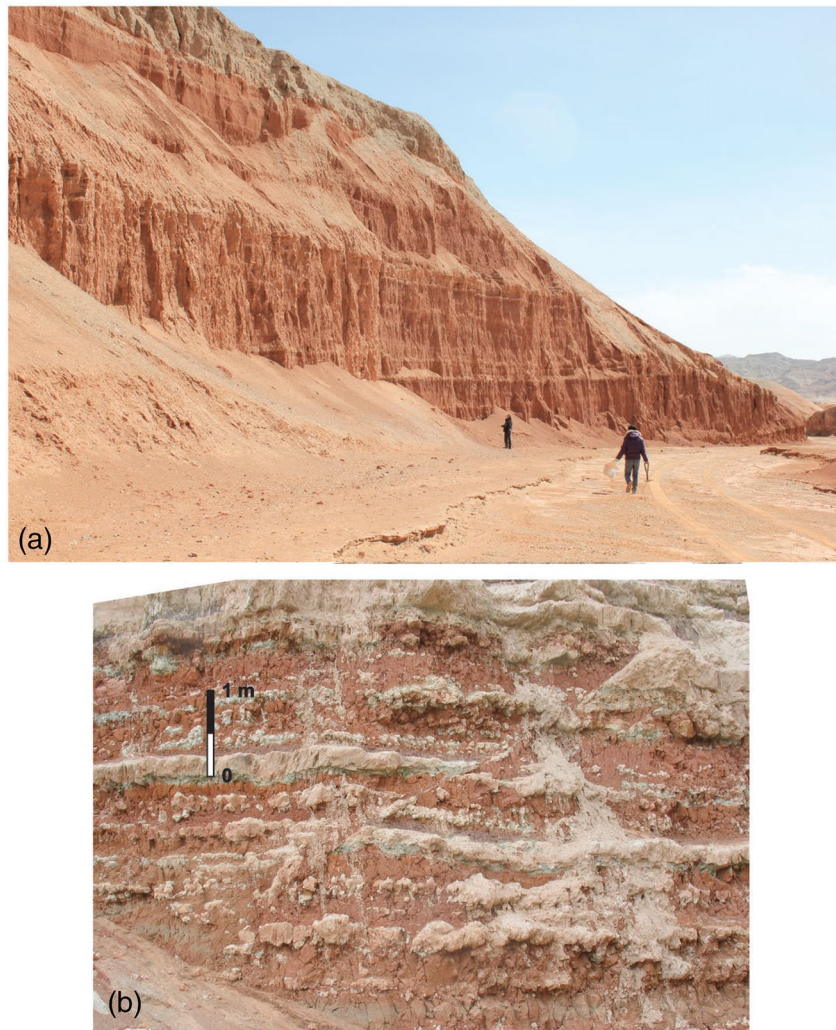


Figure 2. Field photographs of the studied section with pseudobedding in the studied red clay section; (a) distant view, (b) close-up view.

Table 1
Dating of geomagnetic events (geomagnetic excursions or tiny wiggles) in the Altun Shan red clay section

Event number in Figure 2	Geomagnetic chron where the event was located	Age (Ma)	Comments
1	C20n	42.7	Four samples
2 ^a	C20n	42.84	Two samples
3	C20r	44.0	Three samples
4 ^a	C20r	44.37	Three samples
5	C21n	46.7	Nine samples
6	C21n	46.97	Five samples
7	C21r	48.02	Four samples
8	C21r	48.15	Four samples

^aUncertain event because of the small number of representative samples or the weak magnetization.

using an ASC TD-48 furnace housed in a triaxial Helmholtz induction coil system. Thermal demagnetization of natural remanent magnetization was performed in 10–25 °C steps from room temperature to 700 °C.

The measurement of 38 samples in addition to samples reported in Li et al. (2018) enabled us to produce an estimation of age for eight short geomagnetic events. Seven of these geomagnetic events are registered by at least three samples (Table 1). The ages for these events are determined based on our magnetostratigraphic and cyclostratigraphic age model described in Results.

3.3. Spectral Analysis

We used the Matlab code of Torrence and Compo (1998) to perform wavelet analysis to decompose time series into a time-frequency domain. The Morlet wavelet and the background red noise at 95% confidence were applied. A Monte Carlo simulation was used to evaluate the statistical significance of wavelet signal. Background noise for each signal was

estimated using singular spectrum analysis (Torrence & Compo, 1998). Autoregressive (AR) modeling was applied for each noise time series to determine the background noise AR (1) when AR (1) > 0.

3.4. Cyclostratigraphy and Magnetostratigraphy Approach

Cyclostratigraphy uses astronomical cycles to date and interpret sedimentary records (Strasser et al.,). The main orbital cycles are precession, obliquity, and eccentricity; an average sampling rate of one sample per 20 cm allowed us to evaluate eccentricity with main periods of ~400 and 100 kyr. To build our age model that combines magnetostratigraphy and cyclostratigraphy, we started with creating of the visual first-order magnetostratigraphic correlation between the polarity intervals in the study section and the GPTS (Gradstein et al., 2012). Then we converted depth to time for the magnetostratigraphy control points. The middle-late Eocene age of the fossil reported in Wang (2017) and Li et al. (2018) was taken in account in every magnetostratigraphic model. After obtaining the first-order magnetostratigraphic age model, we used our Matlab script where we assigned random nonlinearly spaced ages to every MS data point between each pair of the neighboring magnetostratigraphic control points, and then performed spectral analysis using the Matlab code provided in Torrence and Compo (1998). Each data point ages were reassigned in an iterative manner to produce better match of the resulting wavelet spectra to the expected eccentricity oscillation centered at ~400 kyr. If we did not resolve the 400 kyr cycle in the wavelet spectra we manually produced a different visual magnetostratigraphic correlation with the GPTS and performed the age reassignment to the data points and spectral analysis again. This procedure was repeated several times with all possible magnetostratigraphic correlations. The magnetostratigraphic correlation that produced the best resolved amplitude and width of the 400 kyr eccentricity cycle in the wavelet spectra was chosen as the final solution.

The iterative procedure can be regarded as random stretching and squeezing of the time series between magnetostratigraphic correlation lines, assuming nonlinear changes in the sedimentation rate, until the best resolution of the eccentricity cycles in the spectra was obtained (Rohrhaft, 2012). The random age reassignment between the magnetostratigraphic correlation points was accomplished without impacting the age of these magnetostratigraphic control points. This iterative procedure did not require a reference curve for tuning. The procedure involves a few dozens or hundreds of iterations until a spectral peak of higher amplitude at the target periodicity, the 400 kyr peak in our case, is achieved. The procedure of assigning random ages to the data points between control points necessitates a large number of iterations to produce a robust and stable solution, therefore we used the Westgrid server cluster of Compute Canada.

3.5. Detrending and Filtering

The long-term trends of the Altun Shan MS record and oceanic oxygen isotope $\delta^{18}\text{O}$ compilation (Zachos et al., 2001, 2008) are nonlinear. Therefore, to fit the trends we used a nonlinear locally weighted polynomial regression (a locally weighted scatterplot smoothing, or LOWESS method) using the Matlab software with a smoothing parameter of 0.06 (6% of the data are used in each fitting) for MS and 0.05 for the $\delta^{18}\text{O}$ record.

We built the band-pass frequency filters in Matlab and then applied them to the MS data to highlight the 400 and 100 kyr eccentricity cycles. The filters were centered at 400 kyr and 100 kyr and spanned in the frequency intervals $0.002\text{--}0.0027\text{ kyr}^{-1}$ and $0.008\text{--}0.011\text{ kyr}^{-1}$ correspondingly.

4. Results

Figure 3a illustrates MS and χ_{fd} variations in the study section. The relative amplitudes for both parameters look similar, and the two parameters correlate with the correlation coefficient 0.91; that implies that the MS is largely defined by the signals of SP + SD magnetic particles produced during paleosol formation (Figure 3b). The number of such particles gradually increases toward the bottom of the study section (Figure 3a). Overall, the variation in MS is not high in the section spanning from averages of $\sim 20 \times 10^{-8}\text{ m}^3/\text{kg}$ below 60 m to $\sim 10 \times 10^{-8}\text{ m}^3/\text{kg}$ above.

The results of the demagnetization of our paleomagnetic samples taken to assess the short geomagnetic events are shown in Figures 4 and 5. A secondary low temperature component (LTC) of natural remanent magnetization was removed by thermal demagnetization below 250–300 °C. A high temperature

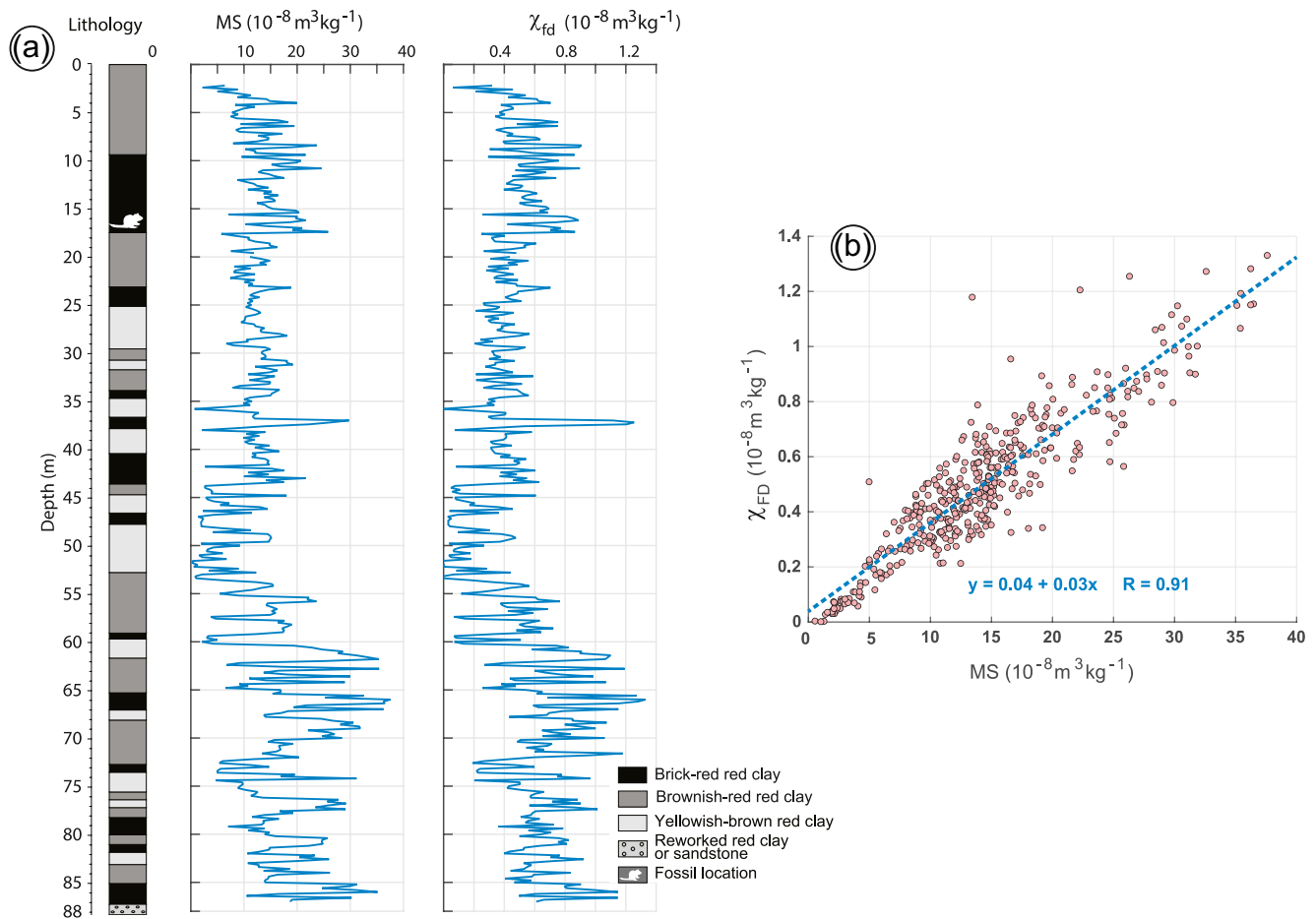


Figure 3. (a) Profiles of magnetic susceptibility (MS) and mass-specific frequency-dependent magnetic susceptibility χ_{fd} versus depth in the Altun Shan section. The lithological column is from Li et al. (2018) (b) Relation between mass-specific frequency-dependent magnetic susceptibility χ_{fd} and low-field magnetic susceptibility (MS). The observed linear correlation between both parameters demonstrates that with increasing magnitude the MS becomes more controlled by the contribution from the fine-grained magnetic fraction, illustrating that the new MS data and χ_{fd} from Li et al. (2018) vary in a generally similar manner. Please note that that the profile is shorter than in Figure 6 because the MS record from the sandstone layers below 87 m is not climate depended and could not be used as the paleoclimate proxy.

component (HTC) is accentuated in the interval between the LTC and 550–600 °C that confirms that magnetite is the main carrier of the remanent magnetization. Most samples have strong magnetization (an order of 10^{-3} A/m and higher) and demonstrate a clear trend toward the origin of the orthogonal projection diagram. The HTC results from additional samples enabled us to assess eight short geomagnetic events, possible cryochrons, that are highlighted in Figure 6 and listed in Table 1. The only sample that had weak magnetization (4.26×10^{-5} A/m) and did not clearly trend toward the origin was sample X-234 from short event 4. The direction of this sample is preserved up to 400 °C during demagnetization, then scatters simultaneously with increasing intensity and MS at higher temperatures, indicating mineralogical changes (most likely magnetite production).

Our final magnetostratigraphic correlation that incorporated the cyclostratigraphic procedure described in Methods is shown in Figure 6. The geomagnetic chrons in the study section range from the top of the chron C23n.1n to the bottom of the chron C18.2n (Fig. 6d, 6e). The MS record showed the long-term climatic trend discussed in Li et al. (2018); therefore, to evaluate the presence of eccentricity cycles in the record, we calculated the long-term trend for the record. The trend is unrelated to the eccentricity cycles and creates large amplitude long period signals (longer than 0.5 Myr) in the amplitude spectra that obscure cycles related to astronomical periodicities (Figures 7a and 7b). We subtracted the long-term trend from the original MS record to extract the higher order variations of the signal related to eccentricity (Figure 7b). The detrending

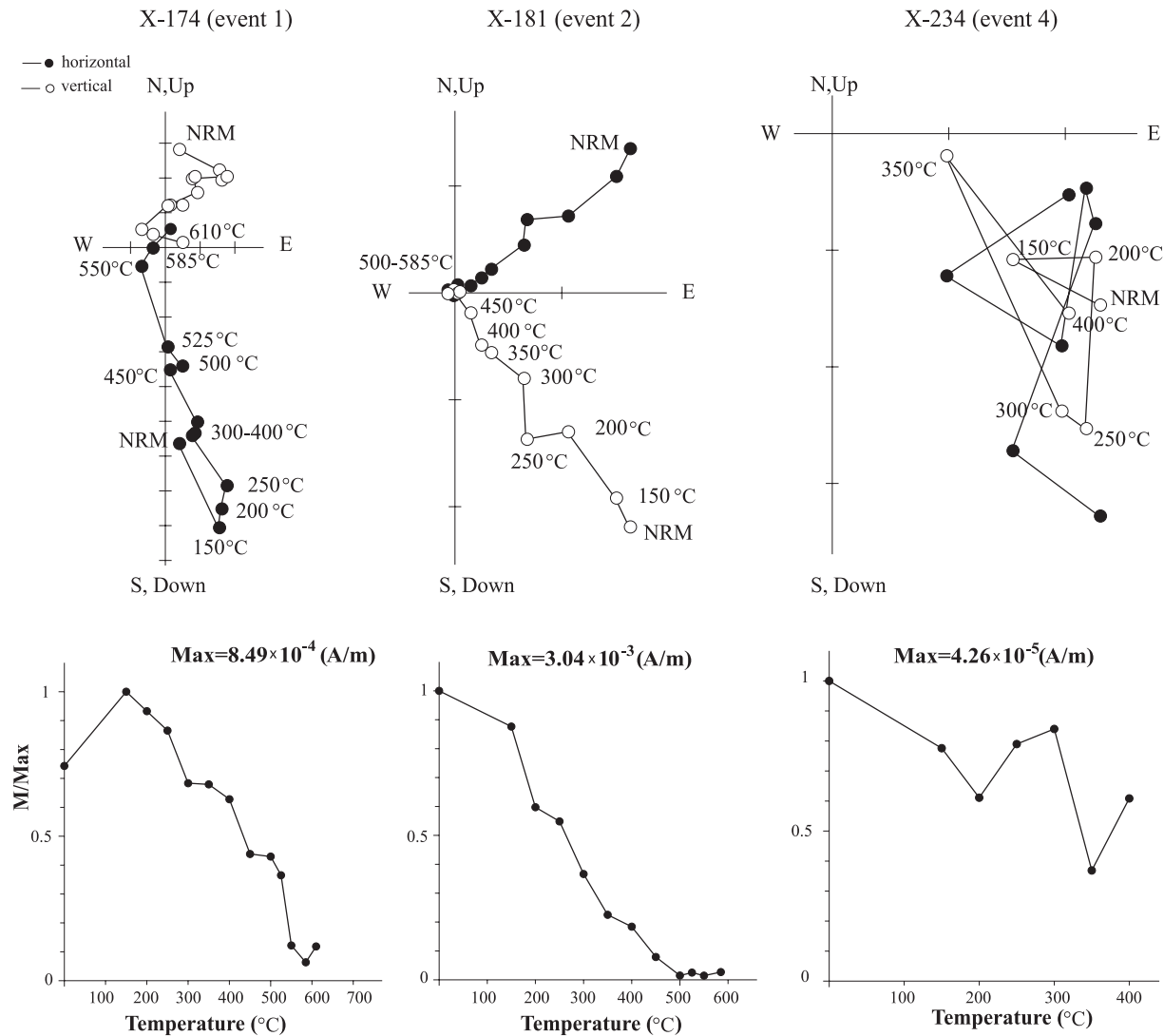


Figure 4. Representative orthogonal vector projections of stepwise thermal demagnetizations of samples from the studied section. Open and closed circles indicate magnetization vectors projected onto the vertical and horizontal planes, respectively.

procedure does not influence the magnetostratigraphic age model. Figures 7c and 7d shows wavelet power spectrum and global wavelet spectrum for the detrended MS record with the 400 kyr cycle resolved in the best possible manner using magnetostratigraphy and cyclostratigraphy approach.

The amplitude of the 400 kyr signal is much stronger than the amplitude of the 100 kyr signal (Figures 7c and 7d); this pattern is similar in Pliocene and Pleistocene red clay records (Anwar et al., 2015; Nie, 2018). Considering sedimentation rate variations in different intervals (Figure 7e), the resolution of the MS record is 15–25 kyr for most of the section, with exceptions of ~42 kyr in the 43.4–45.7 Ma interval and ~55 kyr in the 48.5–49.3 Ma interval (Figure 8). Martinez et al. (2016) showed that having ten samples per precession cycle was preferable for preserving both spectral power and significance level. Therefore, our resolution makes it possible to clearly resolve the 400 kyr eccentricity cycle and to resolve in part the 100 kyr eccentricity cycle. To highlight the presence of the 100 kyr eccentricity cycle, we applied a band-pass filter for both 400 kyr and 100 kyr periodicities (Figure 8). In addition to the dominant 400 kyr cycle, the 100 kyr cycle was persistently present in the filtered MS record.

Our new age model of the Altun Shan red clay section spans from 40.145 to 50.628 Ma and is similar but not identical to the model published in Li et al. (2018) (Figure 3 and Supplementary Figure 10a in Li

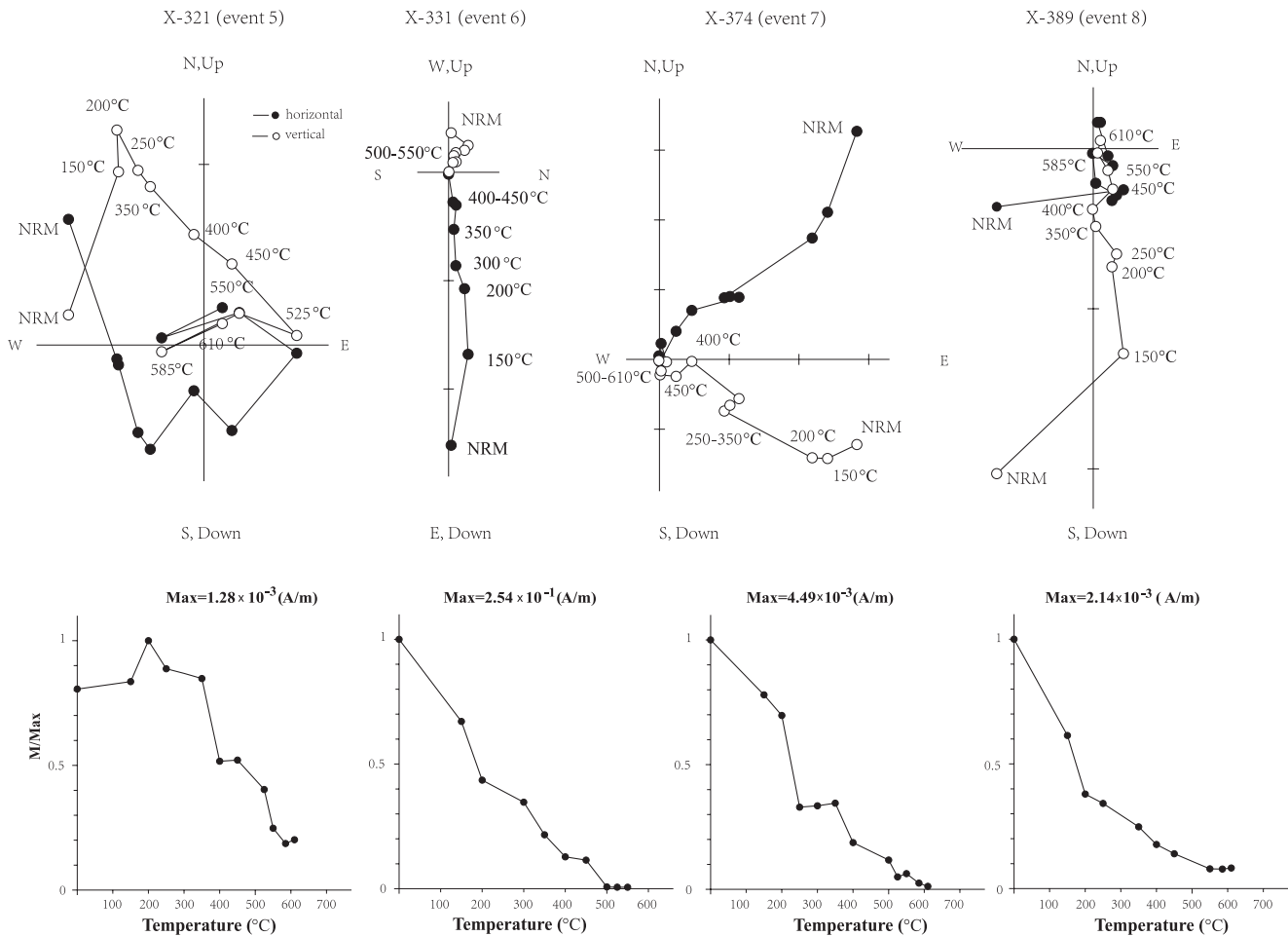


Figure 5. Representative orthogonal vector projections of stepwise thermal demagnetizations for samples from the studied section. Open and closed circles indicate magnetization vectors projected onto the vertical and horizontal planes, respectively.

et al. (2018)), which recorded smoother sedimentation rates. Sedimentation rates of our age model vary reasonably around 8 m/Myr (0.8 cm/kyr) \pm 4 m/Myr (Figure 7e) that is close to typical sedimentation rates (1.1–2.9 cm/kyr) of the Pliocene-late Miocene red clay deposits (Zhang et al., 2018). Nie et al. (2018) showed that increased sedimentation rates in the late Miocene-Pliocene red clay east of Tibet generally corresponded to increased erosion caused by increasing of precipitation caused by the East Asian summer monsoon intensification.

Our procedure is based on the assumption that eccentricity cycles are encoded in our record without any phase lag. Therefore, even though our new age model helps to confirm the correctness of only one magnetostratigraphy age model from three possible age models suggested in Li et al. (2018), there remains a possibility that our tuned age model might be not ideal. For example, Lisiecki (2010) discussed the links between eccentricity forcing and the 100 kyr glacial cycles during the last 5 Myr and showed that phase-locking mechanisms could produce small phase lags of 2.1 kyr between $\delta^{18}\text{O}$ and eccentricity since 1.2 Ma. Certainly, if such small lags existed between our study MS and eccentricity record they could not be resolved as 1 cm represents \sim 1.7 kyr in the Altun Shan section.

Further we verified the ages of eight short polarity events suggested as probable in Li et al. (2018). The stable demagnetization behavior of the majority of samples confirms that short-term intervals between chrons could be pinpointed with at least three samples per event for events 1, 3, 5–8 (Table 1). Events 2 and 4 had less than three samples or weakly magnetized samples. The median age was assigned to these short polarity events based on our new age model (Table 1). Cande and Kent (1995) identified short geomagnetic

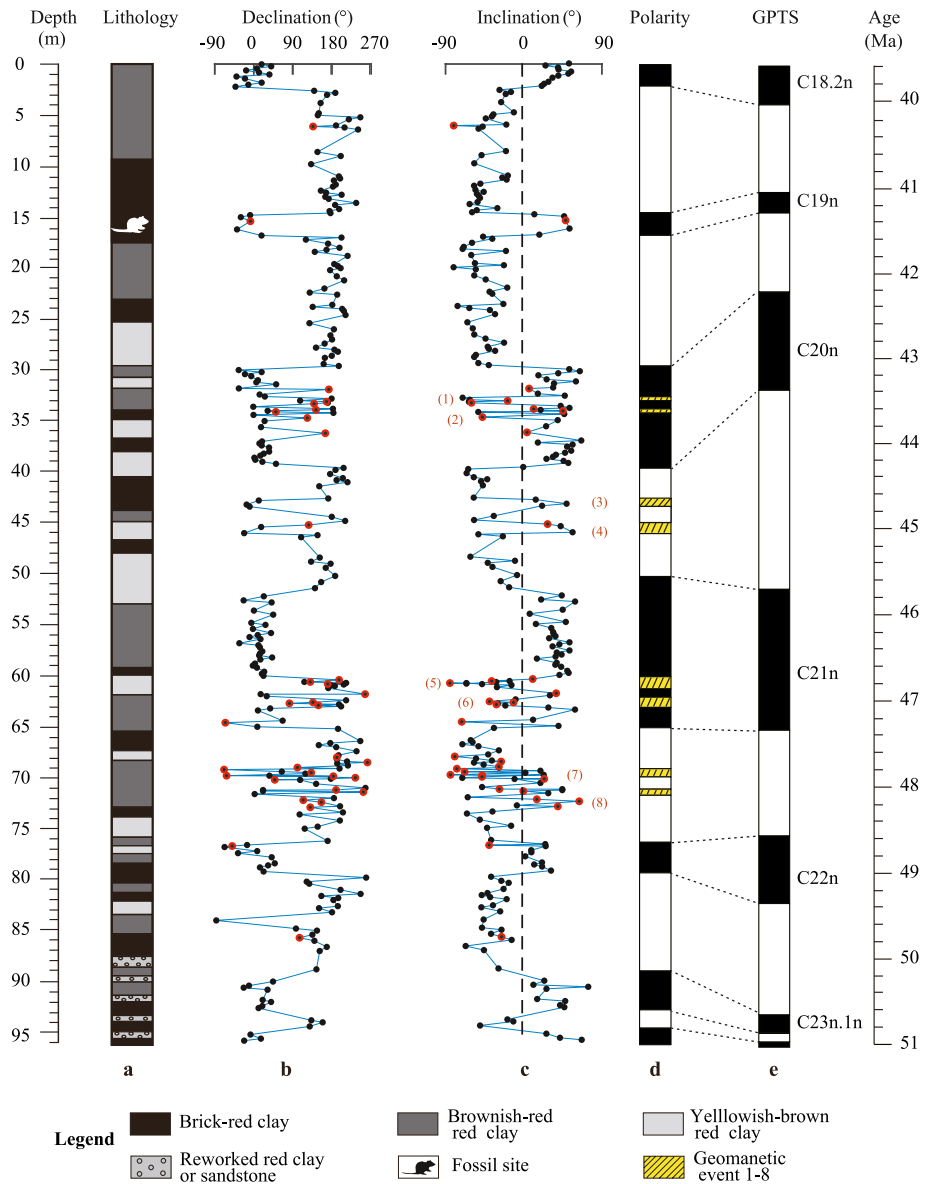


Figure 6. Magnetostratigraphy supported by cyclostratigraphic analysis of the Altun Shan red clay section: (a) lithology, (b) declination, (c) inclination, (d) magnetic polarity, (e) geomagnetic polarity timescale (Gradstein et al., 2012). Red dots indicate samples measured additionally to the number of samples recorded in Li et al. (2018). The lithological column was produced in Li et al. (2018).

events, so called tiny wiggles or cryptochrons, within numerous polarity chrons in the Cenozoic Era. The cryptochrons represent either large amplitude intensity variations in the marine magnetic anomalies, or geomagnetic excursions, or short polarity subchrons. There are no cryptochrons reported between chrons C13r and C24r in the marine magnetic records (Cande & Kent, 1995), therefore, our record provides a possibility to determine short geomagnetic events or geomagnetic excursions in the red clay deposits. The duration of the events in our study are of the same order as cryptochrons. However, to estimate the duration of events accurately in the future, higher density sampling and tuning to obliquity and precession are required to account better for nonlinearity in the sedimentation rate.

We note that recent two geomagnetic polarity time scales that include reassignment of the Eocene chron boundaries (Boullila et al., 2018; Malinverno et al., 2020) slightly differ from each other and the GPTS from Gradstein et al. (2012) that was used by Li et al. (2018). Differences for the chrons 19n–20r are larger (up to a

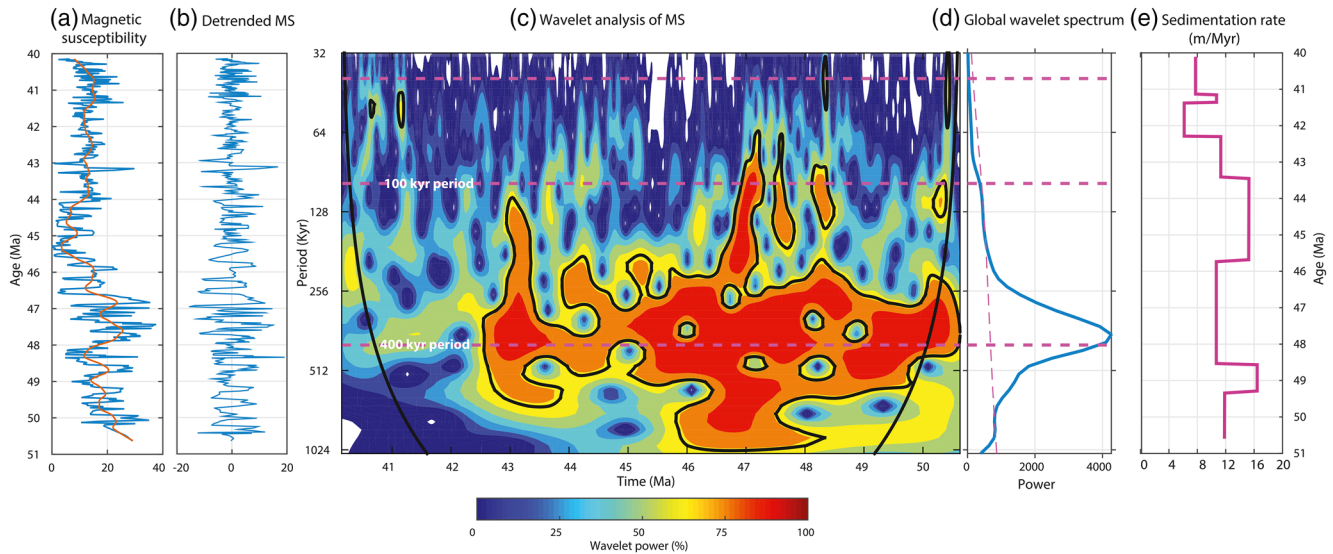


Figure 7. Wavelet analysis of the magnetic susceptibility of Altun Shan red clay samples deposited between 40 and 51 Ma and sedimentation rates. (a) Magnetic susceptibility ($10^{-8} \text{ m}^3/\text{kg}$) (blue line), long-term trend of magnetic susceptibility (red line). (b) Detrended magnetic susceptibility; wavelet power is shown in %; the thick black line indicates a 5% significance level, the thin black cone is the contour of influence, and the horizontal dashed lines correspond to Milankovitch cycles; (d) Fourier power spectrum; the magenta dashed line is the level of the mean red noise spectrum with a lag of 0.7; (e) Rate of sedimentation in the Altun Shan section based on paleomagnetic and cyclostratigraphic results.

few 100 kyrs) and the differences for the chrons 21–23 are relatively small (around 100–200 kyrs). We chose the GPTS of Gradstein et al. (2012) for our magnetostratigraphic correlation because it is the same GPTS as in Li et al. (2018). The magnetostratigraphic age assignment and duration of the cryochrons would vary if we chose another GPTS.

5. Discussion

Figure 8 illustrates a comparison of the band-pass filtered MS time series with the eccentricity variations (Laskar et al., 2011). The 400 and 100 kyr eccentricity periodicities and their amplitudes are similar for both time series. Although many features could be visually correlated, the 100 kyr eccentricity cycle is distorted

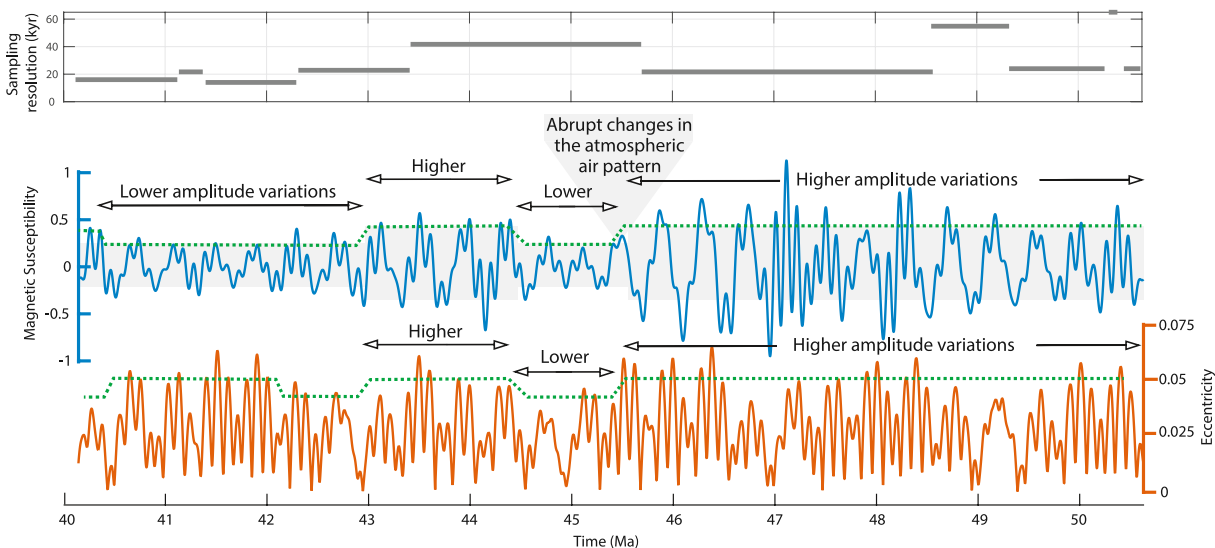


Figure 8. Comparison of the band-pass filtered, detrended, normalized magnetic susceptibility record and eccentricity variations 40–51 Ma in the Altun Shan red clay section; filters are centered at 400 and 100 kyr. Changes in amplitude mark the beginning and the end of middle Eocene cooling events 45.5–44 Ma.

in the lower sampling resolution intervals. Higher and lower amplitude signals for the 400 kyr cycles alternate noticeably in the filtered MS record. Amplitudes in the 400 and 100 kyr eccentricity cycles decreased around 45.5 Ma and then increased around 44.5 Ma following the amplitude changes in the eccentricity signal. This might indicate that the intensity of atmospheric moisture versus the aridity changes in the study area was paced by the eccentricity signal between 51 and 43 Ma. The amplitudes of the MS signal and eccentricity differ at the interval 43–40 Ma, suggesting that factors in addition to the eccentricity changes could play roles in the MS signal amplification and reduction. Meijer et al. (2019) showed a sudden retreat of the proto-Paratethys Sea from the central part of Asia north of the Tibetan Plateau, commencing around 44–43 Ma that could be one of the factors changing the dominance of the eccentricity pacing in Altun Shan. However, other mechanisms that explain the observed amplitude mismatch between orbital forcing and climatic response are also possible. For example, Lisiecki (2010) suggested that for the last 5 Myr, particularly during the marine isotope stage 11, the amplitude mismatch between eccentricity and oxygen isotope curve could depend on the strong precession forcing that disrupted the internal climate feedbacks for the 100 kyr glacial cycle. Nie (2011) showed that Chinese loess records between 3 and 1 Ma were amplitude coupled with benthic oxygen and carbon isotope records at the 100 kyr band, but not with the 100 kyr eccentricity forcing. He concluded that the late Pleistocene 100 kyr climate cycles could not result solely from the orbital oscillations, though the mechanism responsible for it is not known. At the same time, these suggestions and corresponding hypothetical mechanisms for the icehouse world cannot be directly extrapolated to the ice-free Middle Eocene world.

The global record of the oxygen isotope $\delta^{18}\text{O}$ in the Eocene is characterized by a long cooling trend between 49 and 34 Ma that began after the early Eocene climatic optimum (53–49 Ma) (Zachos et al., 2001, 2008). The cooling trend coincides with the long-term trend of mass-specific frequency-dependent magnetic susceptibility χ_{fd} in the Altun Shan section, as proposed in Li et al. (2018). On the basis of marine microfossil and organic geochemical records, Bijl et al. (2013) suggested that the earliest flow of an Antarctic counter current began ~49–50 Ma from the west via a southern aperture in the Tasmanian Antarctic gateway. This oceanic current led to a cooling of Antarctic surface waters and coasts in the apparent absence of near equatorial cooling. Chilled water was transported through deep convection to middle latitudes, causing a long-term global cooling of the ocean (Bijl et al., 2013).

The $\delta^{18}\text{O}$ cooling trend was disturbed by the middle Eocene climatic optimum (MECO), a short warming event around 42–40 Ma that corresponded to an increase in global temperatures (Bohaty et al., 2003, 2009). However, the cooling trend was not uniform and changed anomalously around 45 Ma (Figure 9a). To evaluate the duration of the cooling anomaly in the middle Eocene we constructed a long-term trend of the $\delta^{18}\text{O}$ global record (see section 2). We subtracted the trend from the primary $\delta^{18}\text{O}$ record to highlight the cooling maximum around 45.5–44 Ma (Figure 9b). This one and a half million yearlong cooling recorded in the detrended $\delta^{18}\text{O}$ profile coincides with the most notable feature in our Altun Shan MS record—the aridity interval between 45.5 and 44 Ma (Figure 9c). Indeed, the cooling trend indicated in the global oxygen isotope record started after the opening of the Tasmanian Antarctic gateway, ~50 Ma (Figure 9d), and reached its maximum between ~45.5 and 44 Ma, as registered by detrended $\delta^{18}\text{O}$. Individual records that were used to construct the benthic foraminifer $\delta^{18}\text{O}$ record (Zachos et al., 2008) show considerable differences because of their dependency on the deepwater mass in different latitudes and uncertainties in the age models. Nevertheless, the one and a half million yearlong cooling interval appears in the sea surface temperature records (Bijl et al., 2009) and the $\delta^{18}\text{O}$ -based ice-free deep-ocean temperature stack (Cramwinckel et al., 2018). Figure 9e shows the sea surface temperature (SST) reconstructed from the ODP Leg 189 Site 1172 at the east Tasmanian plateau that represents a high latitude record of the Pleistocene and Eocene (~65°S) (Bijl et al., 2009). The middle Eocene cooling (MEC) is visually pronounced in the SST record and coincides with the aridity interval in the Altun Shan MS record, suggesting a teleconnection between the MEC and the middle Eocene aridity (MEA) event. Tripathi and Darby (2018) demonstrated the presence of episodic glaciation on Greenland that was synchronous with ice-rafting from circum-Arctic sources in the middle Eocene. The earliest episodic glaciations registered between ~45.5 and 42 Ma (Figures 9c and 9d) coincide with the increased aridity in Altun Shan.

Rugenstein and Chamberlain (2018) compiled extensive pedogenic and lacustrine carbonate isotope data for the last 55 Myr. The stable oxygen $\delta^{18}\text{O}$ record was used to reconstruct the large-scale atmospheric

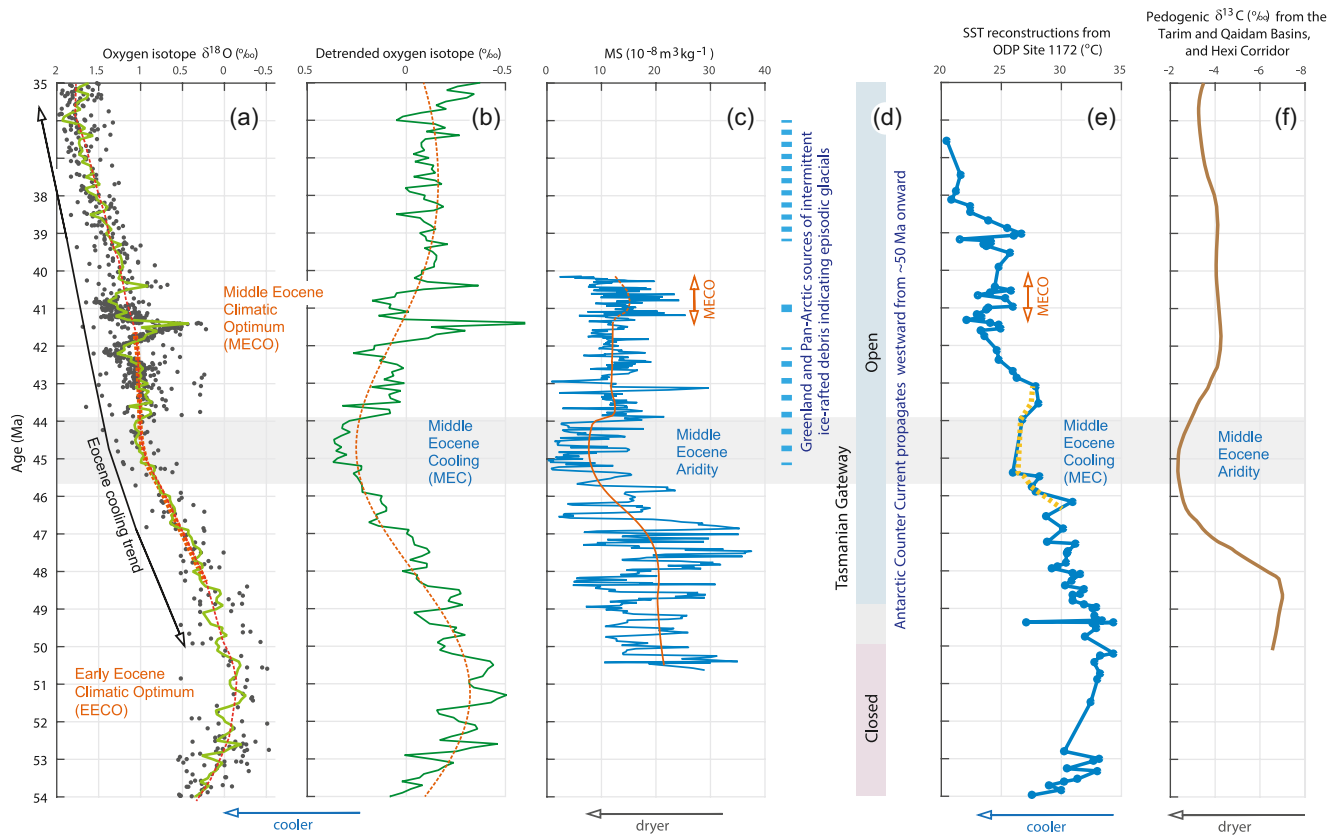


Figure 9. Comparison of the global and Altun Shan middle Eocene paleoclimate records. (a) Oceanic record of oxygen isotope $\delta^{18}\text{O}$ (Zachos et al., 2008); the dots represent the original data, the green line is a smoothed record, the dotted red line is the long-term trend. (b) Detrended and normalized oceanic record of oxygen isotope $\delta^{18}\text{O}$; the green line is the smoothed record, the dotted orange line is the long-term trend. (c) This study's magnetic susceptibility record from Altun Shan (blue line) and the long-term trend (orange line). (d) Timelines of the Greenland and Pan-Arctic sources of intermittent ice-rafted debris indicating episodic glacials (Tripathi and Darby, 2018) and of the Tasmanian Gateway opening (Bijl et al., 2013). (e) SST (sea surface temperature) reconstructions from ODP Site 1172 (east Tasmanian plateau) (Bijl et al., 2009); the yellow dashed line highlights the middle Eocene cooling (MEC) interval. (f) A compilation of the pedogenic $\delta^{13}\text{C}$ from the Tarim Basin, the Qaidam Basin, and the Hexi Corridor as an indicator of moisture content in the soil over geological time (Rugenstein and Chamberlain, 2018). The horizontal gray line corresponds to the MEC (middle Eocene cooling) and the MEA (middle Eocene aridity) proposed in this study.

circulation and the $\delta^{13}\text{C}_c$ carbon isotope record from pedogenic carbonate was used to reconstruct the primary pedogenic productivity that depends on atmospheric moisture. The $\delta^{18}\text{O}$ compilation indicated that the atmospheric circulation 55 Ma was generally similar to that of today. The moisture reconstructions showed that the Central Asian paleoclimate changes were tightly controlled by the global climate and by interactions of the midlatitude westerlies with the Tian Shan and Altai mountains rather than by changes in the height or extent of the Tibetan Plateau or the Paratethys. Figure 9f shows pedogenic carbonate $\delta^{13}\text{C}_c$ time series compilations for the Tarim Basin, the Qaidam Basin, and the Hexi Corridor. The increase in $\delta^{13}\text{C}_c$ around 46–44 Ma indicates a decrease in pedogenic productivity as a result of decreased basin-wide moisture. Our Altun Shan study area is situated on the border between Tarim and Qaidam basins, therefore, it is not surprising that the red clay therein also recorded a decrease in moisture, indicating a maximum regional aridity between 45.5 and 44 Ma.

6. Conclusions

We used cyclostratigraphy, available paleontological dating, and a correlation of the polarity pattern to the geomagnetic polarity time scale (GPTS) to reassess the age model of the Altun Shan in the middle Eocene section near northeastern Tibet previously described in Li et al. (2018). Our new age model confirms and refines one from three age models that was suggested as the preferable model in Li et al. (2018). By nonlinear

stretching and squeezing of the magnetic susceptibility time series between the top and bottom of individual chrons, we resolved 400 and 100 kyr eccentricity cycles. It is shown that the amplitudes of the MS cycles are paced by eccentricity amplitude changes for most of the study interval. We assess the median age of eight short geomagnetic polarity events, probable cryochrons. Our MS data reveal a one and a half million yearlong aridity in the Altun Shan section in the middle Eocene between 45.5 and 44 Ma. The aridity episode coincides with the decrease in atmospheric moisture expressed in the pedogenic $\delta^{13}\text{C}_c$ records from Tarim and Qaidam basins and the Hexi Corridor that surround the Altun Shan study area. The one and a half million yearlong aridity episode corresponds to the cooling interval expressed in the global $\delta^{18}\text{O}$ compilation and to the first appearance of ice-rafted debris from Greenland and Pan-Arctic sources, indicating episodic glacials in the near polar areas. Therefore, we propose that the episodic cooling and aridity events took place in many parts of the world between ~45.5 and 44 Ma.

Data Availability Statement

The data are available at <http://doi.org/10.5281/zenodo.4448449>.

Acknowledgments

This work was cosupported by the Natural Sciences and Engineering Research Council of Canada (NSERC Grant RGPIN-2019-04780) and the National Natural Science Foundation of China (41772027, 41372037, 41972035, 41950410574). We thank F. Pan for help in the field and M. Craig for editing the manuscript. We thank four anonymous reviewers and an associate editor for their valuable comments that helped to substantially improve the manuscript. Vadim A. Kravchinsky is the corresponding author, Rui Zhang and Vadim A. Kravchinsky prepared the manuscript and processed, analyzed, and interpreted the data. Jianxing Li undertook sampling and provided geological descriptions, Jie Qin helped with the data processing, Avto Goguitchaichvili participated in the discussion and interpretation of the results. Cyclostratigraphic cycles were computed using the Westgrid server cluster of Compute Canada.

References

- An, Z., Kutzbach, J. E., Prell, W. L., & Porter, S. C. (2001). Evolution of Asian monsoons and phased uplift of the Himalaya-Tibetan plateau since Late Miocene times. *Nature*, *411*(6833), 62–66. <https://doi.org/10.1038/35075035>
- Anwar, T., Kravchinsky, V. A., & Zhang, R. (2015). Magneto- and cyclostratigraphy in the red clay sequence: New age model and paleoclimatic implication for the eastern Chinese Loess Plateau. *Journal of Geophysical Research: Solid Earth*, *120*, 6758–6770. <https://doi.org/10.1002/2015JB012132>
- Bijl, P. K., Bendle, J. A., Bohaty, S. M., Pross, J., Schouten, S., Tauxe, L., et al. (2013). Eocene cooling linked to early flow across the Tasmanian Gateway. *Proceedings of the National Academy of Sciences of the United States of America*, *110*(24), 9645–9650. <https://doi.org/10.1073/pnas.1220872110>
- Bijl, P. K., Schouten, S., Sluijs, A., Reichert, G. J., Zachos, J. C., & Brinkhuis, H. (2009). Early Palaeogene temperature evolution of the southwest Pacific Ocean. *Nature*, *461*(7265), 776–779. <https://doi.org/10.1038/nature08399>
- Bohaty, S. M., & Zachos, J. C. (2003). Significant Southern Ocean warming event in the late middle Eocene. *Geology*, *31*(11), 1017–1020. <https://doi.org/10.1130/G19800.1>
- Bohaty, S. M., Zachos, J. C., Florindo, F., & Delaney, M. L. (2009). Coupled greenhouse warming and deep-sea acidification in the middle Eocene. *Paleoceanography*, *24*, PA2207. <https://doi.org/10.1029/2008PA001676>
- Boullila, S., Vahlenkamp, M., De Vleeschouwer, D., Laskar, J., Yamamoto, Y., Pälike, H., et al. (2018). Towards a robust and consistent middle Eocene astronomical timescale. *Earth and Planetary Science Letters*, *486*, 94–107. <https://doi.org/10.1016/j.epsl.2018.01.003>
- Cande, S. C., & Kent, D. V. (1995). Revised calibration of the geomagnetic polarity timescale for the Late Cretaceous and Cenozoic. *Journal of Geophysical Research: Solid Earth*, *100*(B4), 6093–6095. <https://doi.org/10.1029/94jb03098>
- Cramwinckel, M. J., Huber, M., Kocken, I. J., Agnini, C., Bijl, P. K., Bohaty, S. M., et al. (2018). Synchronous tropical and polar temperature evolution in the Eocene. *Nature*, *559*(7714), 382–386. <https://doi.org/10.1038/s41586-018-0272-2>
- Evans, M. E., Wang, Y., Rutter, N., & Ding, Z. (1991). Preliminary magnetostratigraphy of the red clay underlying the loess sequence at Baoji, China. *Geophysical Research Letters*, *18*(8), 1409–1412. <https://doi.org/10.1029/91gl01800>
- Gradstein, F. M., Ogg, J. G., Schmitz, M., & Ogg, G. (Eds.). (2012). *The geologic time scale* (pp. 1145). Boston, MA: Elsevier.
- Laskar, J., Fienga, A., Gastineau, M., & Manche, H. (2011). La2010: A new orbital solution for the long-term motion of the Earth. *Astronomy & Astrophysics*, *532*, A89. <https://doi.org/10.1051/0004-6361/201116836>
- Li, J., Yue, L., Pan, F., Zhang, R., Guo, L., Xi, R., & Guo, L. (2014). Intensified aridity of the Asian interior recorded by the magnetism of red clay in Altun Shan, NE Tibetan Plateau. *Palaeogeography, Palaeoclimatology, Palaeoecology*, *411*, 30–41.
- Li, J. X., Yue, L. P., Roberts, A. P., Hirt, A. M., Pan, F., Guo, L., et al. (2018). Global cooling and enhanced Eocene Asian mid-latitude interior aridity. *Nature communications*, *9*(1), 1–8. <https://doi.org/10.1038/s41467-018-05415-x>
- Lisiecki, L. E. (2010). Links between eccentricity forcing and the 100,000-year glacial cycle. *Nature Geoscience*, *3*(5), 349–352. <https://doi.org/10.1038/ngeo828>
- Malinverno, A., Quigley, K. W., Staro, A., & Dyment, J. (2020). A late cretaceous-eocene geomagnetic polarity timescale (MQSD20) that steadies spreading rates on multiple mid-ocean ridge flanks. *Journal of Geophysical Research: Solid Earth*, *125*, e2020JB020034. <https://doi.org/10.1029/2020JB020034>
- Martinez, M., Kotov, S., De Vleeschouwer, D., Pas, D., & Pälike, H. (2016). Testing the impact of stratigraphic uncertainty on spectral analyses of sedimentary series. *Climate of the Past*, *12*, 1765–1783. <https://cp.copernicus.org/articles/12/1765/2016/>
- Meijer, N., Dupont-Nivet, G., Abels, H. A., Kaya, M. Y., Licht, A., Xiao, M., et al. (2019). Central Asian moisture modulated by proto-Paratethys Sea incursions since the early Eocene. *Earth and Planetary Science Letters*, *510*, 73–84. <https://doi.org/10.1016/j.epsl.2018.12.031>
- Nie, J. (2011). Coupled 100-kyr cycles between 3 and 1 Ma in terrestrial and marine paleoclimatic records. *Geochemistry, Geophysics, Geosystems*, *12*, Q10Z32. <https://doi.org/10.1029/2011GC003772>
- Nie, J. (2018). The Plio-Pleistocene 405-kyr climate cycles. *Palaeogeography, Palaeoclimatology, Palaeoecology*, *510*, 26–30. <https://doi.org/10.1016/j.palaeo.2017.07.022>
- Nie, J., Jackson, M., King, J., & Fang, X. (2013). Characterizing the superparamagnetic grain distribution of Chinese red-clay sequences by thermal fluctuation tomography. *Global and Planetary Change*, *110*, 364–367. <https://doi.org/10.1016/j.gloplacha.2013.04.012>
- Nie, J., King, J. W., & Fang, X. (2007). Enhancement mechanisms of magnetic susceptibility in the Chinese red - clay sequence. *Geophysical Research Letters*, *34*, L19705. <https://doi.org/10.1029/2007GL031430>
- Nie, J., King, J. W., & Fang, X. (2008). Tibetan uplift intensified the 400 ky signal in paleoclimate records at 4 Ma. *Geological Society of America Bulletin*, *120*(9–10), 1338–1344. <https://doi.org/10.1130/B26349.1>

- Nie, J., Pullen, A., Garzzone, C. N., Peng, W., & Wang, Z. (2018). Pre-Quaternary decoupling between Asian aridification and high dust accumulation rates. *Science Advances*, *4*(2), eaao6977.
- Rohrhaft, K. J. (2012). *Time series processing: Stratigraphic and paleoclimatic implications* (M.Sc. thesis, pp. 80). Edmonton, AB: University of Alberta.
- Rugenstein, J. K. C., & Chamberlain, C. P. (2018). The evolution of hydroclimate in Asia over the Cenozoic: A stable-isotope perspective. *Earth-Science Reviews*, *185*, 1129–1156. <https://doi.org/10.1016/j.earscirev.2018.09.003>
- Sun, Y., An, Z., Clemens, S. C., Bloemendal, J., & Vandenberghe, J. (2010). Seven million years of wind and precipitation variability on the Chinese Loess Plateau. *Earth and Planetary Science Letters*, *297*(3–4), 525–535. <https://doi.org/10.1016/j.epsl.2010.07.004>
- Sun, Y., Clemens, S. C., An, Z., & Yu, Z. (2006). Astronomical timescale and palaeoclimatic implication of stacked 3.6-Myr monsoon records from the Chinese Loess Plateau. *Quaternary Science Reviews*, *25*(1–2), 33–48. <https://doi.org/10.1016/j.quascirev.2005.07.005>
- The Geological Survey Team of the Xinjiang Uygur Autonomous Region (1981). *Regional Map and Report of the Geology and Mineral Resources for the Soerkuli sheet at the scale of 1:200,000* (in Chinese). Urumqi. The Geological Survey Team of the Xinjiang Uygur Autonomous Region (in Chinese).
- Torrence, C., & Compo, G. P. (1998). A practical guide to wavelet analysis. *Bulletin of the American Meteorological Society*, *79*(1), 61–78. [https://doi.org/10.1175/1520-0477\(1998\)079<0061:APGTWA>2.0.CO;2](https://doi.org/10.1175/1520-0477(1998)079<0061:APGTWA>2.0.CO;2)
- Tripati, A., & Darby, D. (2018). Evidence for ephemeral middle Eocene to early Oligocene Greenland glacial ice and pan-Arctic sea ice. *Nature communications*, *9*(1), 1–11. <https://doi.org/10.1038/s41467-018-03180-5>
- Vandenberghe, J., Lu, H., Sun, D., van Huissteden, J. K., & Konert, M. (2004). The late Miocene and Pliocene climate in East Asia as recorded by grain size and magnetic susceptibility of the Red Clay deposits (Chinese Loess Plateau). *Palaeogeography, Palaeoclimatology, Palaeoecology*, *204*(3–4), 239–255. [https://doi.org/10.1016/S0031-0182\(03\)00729-6](https://doi.org/10.1016/S0031-0182(03)00729-6)
- Wang, B. (2017). Discovery of *Yuomys* from Altun Shan, Xinjiang, China. *Vertebrata Palasiatica*, *55*, 227–232.
- Zachos, J., Pagani, M., Sloan, L., Thomas, E., & Billups, K. (2001). Trends, rhythms, and aberrations in global climate 65 Ma to present. *Science*, *292*(5517), 686–693. <https://doi.org/10.1126/science.1059412>
- Zachos, J. C., Dickens, G. R., & Zeebe, R. E. (2008). An early Cenozoic perspective on greenhouse warming and carbon-cycle dynamics. *Nature*, *451*(7176), 279–283. <https://doi.org/10.1038/nature06588>
- Zhang, R., Kravchinsky, V. A., Anwar, T., Yue, L., Li, J., & Jiao, J. (2018). Comment on “Late Miocene-Pliocene Asian monsoon intensification linked to Antarctic ice-sheet growth”. *Earth and Planetary Science Letters*, *503*(2018), 248–251. <https://doi.org/10.1016/j.epsl.2018.08.033>
- Zhao, G., Han, Y., Liu, X., Chang, L., Lü, B., Chen, Q., et al. (2016). Can the magnetic susceptibility record of Chinese Red Clay sequence be used for palaeomonsoon reconstructions? *Geophysical Journal International*, *204*(3), 1421–1429. <https://doi.org/10.1093/gji/ggv510>
- Zhao, H., Qiang, X., Xu, X., & Sun, Y. (2020). Iron oxide characteristics of the Chinese loess-red clay sequences and their implications for the evolution of the East Asian summer monsoon since the Late Oligocene. *Palaeogeography, Palaeoclimatology, Palaeoecology*, *543*, 109604. <https://doi.org/10.1016/j.palaeo.2020.109604>